NANO LETTERS

pubs.acs.org/NanoLett Letter

Coherent Hole Transport in Selective Area Grown Ge Nanowire Networks

Santhanu Panikar Ramanandan,[#] Petar Tomić,[#] Nicholas Paul Morgan, Andrea Giunto, Alok Rudra, Klaus Ensslin, Thomas Ihn, and Anna Fontcuberta i Morral*

Cite This: *Nano Lett.* 2022, 22, 4269−4275 Read Online

ACCESS | Metrics & More | Article Recommendations | Supporting Information

ABSTRACT: Holes in germanium nanowires have emerged as a realistic platform for quantum computing based on spin qubit logic. On top of the large spin−orbit coupling that allows fast qubit operation, nanowire geometry and orientation can be tuned to cancel out charge noise and hyperfine interaction. Here, we demonstrate a scalable approach to synthesize and organize Ge nanowires on silicon (100)-oriented substrates. Germanium nanowire networks are obtained by selectively growing on nanopatterned slits in a metalorganic vapor phase epitaxy system. Low-temperature electronic transport measurements are performed on nanowire Hall bar devices revealing high hole doping of ∼10^{18} cm^{-3} and mean free path of ∼10 nm. Quantum diffusive transport phenomena, universal conductance fluctuations, and weak antilocalization are revealed through magneto transport measurements yielding a coherence and a spin−orbit length of the order of 100 and 10 nm, respectively.

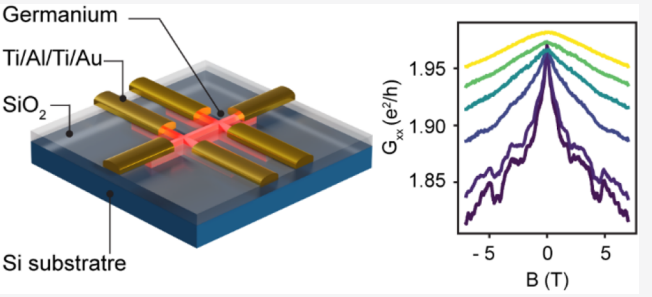

KEYWORDS: *Germanium, nanowire networks, selective area epitaxy, weak antilocalization, spin−orbit interaction*

Holes in germanium nanowires (NWs) are predicted to be a promising platform for spin-qubit-based quantum computing due to their strong spin−orbit interaction (SOI) and low susceptibility to hyperfine interaction.[1−5] The strong SOI of holes enables fast and electrical manipulation of qubits, while the low susceptibility to hyperfine interactions ensures long coherence lifetimes. Of particular interest for nanowires is the possibility of tuning the shape and crystal orientation, which can result in the cancellation of the influence of charge noise and hyperfine interaction on coherence.[6] Thanks to these exhaustive and convenient properties, ultrafast and electrically controlled hole-spin qubits in VLS-grown Ge/Si core/shell nanowires and in self-assembled Ge-hut wires have been demonstrated.[7,8]

Despite the advances in hole-spin qubits in Ge nanowires, the scalability of nanowire-based devices is a major challenge. The ability to grow isolated and connected nanowires with a high degree of controllability in geometry and crystal phase is a prerequisite for NW-based device applications. Although free-standing nanowires grown by VLS methods can form networks,[9−11] the process is inherently not scalable because the grown semiconductor nanowires must be transferred from the growth substrate to an alternate substrate to fabricate the devices. In addition, VLS growth of nanowires is not compatible with existing CMOS technology due to the use of Au catalysts.[12] A more scalable approach is to directly integrate semiconductor nanowires and their networks on a Si substrate in a planar configuration as has been demonstrated with III−Vs.[13−16] To the best of our knowledge, in-plane growth of germanium nanowires on a Si substrate has been limited to the site-controlled growth of so-called "Ge-hut wires" (HWs) using molecular beam epitaxy.[17] Katsaros and colleagues have demonstrated germanium HWs with a strong and tunable SOI obtained along the edges of trenches defined by electron beam lithography and reactive ion etching (RIE). A drawback of this approach is that Ge-HWs are limited to <100> crystallographic orientations and to Si (100) substrates. Since the SOI in Ge NWs is predicted to be strongly dependent on the relative orientation of the NWs with respect to the substrate,[6,18] flexibility in the selection of growth substrate and NW orientation is beneficial to investigate the properties of holes in these structures.

A reliable and scalable strategy to obtain in-plane nanowires is the selective area growth approach (SAG).[13,19] Here, the growth of the semiconductor material is limited to openings in a selective mask, typically SiO_2. The openings are obtained by patterning the mask and uncovering (nanoscale) regions of the

Received: January 27, 2022
Revised: April 23, 2022
Published: May 4, 2022

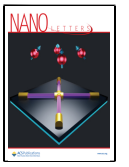

https://doi.org/10.1021/acs.nanolett.2c00358
Nano Lett. 2022, 22, 4269−4275

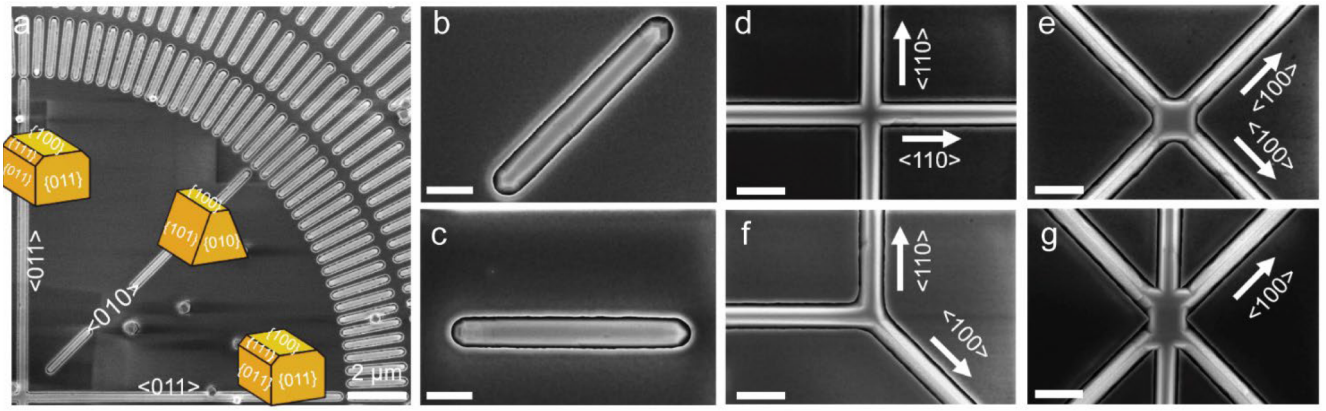

Figure 1. In-plane Ge nanowires grown on Si (100) substrate. (a) Top view SEM image of Ge NWs grown along different crystallographic direction. SEM micrographs of NWs grown along highly symmetric crystallographic orientations, that is, (b) <100> and (c) <110> directions. SEM micrographs of in-plan NW junctions (d) <110>/<110> type, (e) <100>/<100> type, (f) <100>/<110> type and (g) <100> /<110>/<100> type. Scale bar shown in panels b–g indicate 200 nm.

crystalline substrate. Under optimized growth conditions, such as the precursor flow rate and growth temperature, the semiconductor material deposits only in the nonmasked regions. The low sticking coefficient of adatoms on the dielectric mask compared to the substrate ensures the selectivity of the growth.[20] Thus, the position and in-plane disposition of the nanowires can be lithographically defined prior to growth. This allows reducing the defects arising due to the faceting of the NWs by orienting them along highly symmetric crystallographic directions.[21] Furthermore, the nanoscale nature of the SAG also helps in lowering the density of the defects formed during the integration of lattice mismatched materials.[22] Threading dislocations formed at the interface of the heterostructure are blocked by the walls of the mask defining the nanoscale openings, leaving the upper part of the NW free of defects (aspect ratio trapping).[23−25] Most previous SAG studies have focused on the growth of high-quality III−V nanowires and their networks.[13,19,25−27] While there is some work on epitaxial lateral overgrowth of Ge thin films,[28−30] to the best of our knowledge there is no report on the SAG of in-plane germanium nanowires and networks on Si.

In this Letter, as a first step toward realizing scalable spin qubits, we demonstrate the SAG of in-plane germanium nanowires and their networks on Si (100) substrates. Magneto-transport measurements through the nanowire at low temperature indicated phase coherent transport and weak antilocalization. The observed properties make such NWs promising candidates for future quantum information processing schemes.

It is well-known that in SAG, the shape and crystalline orientation of the unmasked regions (from now on referred to as slits) affect the geometry, microstructure, and size of the final nanostructure.[21] This is the result of energy minimization for the stable facet formation as well as kinetics that define preferential growth directions. Our study starts by providing an overview of the effect of slit orientation on the shape of the individual Ge NWs as well as their junctions. To do so, we defined rectangular slits of different sizes, and orientations on an intrinsically doped Si (100) substrate. The mask consists of 175 nm thick thermally grown SiO_2. Ge nanowires were grown inside these nanoscale slits by metal−organic vapor phase epitaxy (MOVPE). We used isobutyl germane as a precursor species and N_2 as the carrier gas. A detailed description of the substrate patterning and growth procedure can be found in the Supporting Information (SI).

The design flexibility of the SAG process for in-plane Ge NWs is illustrated in Figure 1. Figure 1a−g provide top-view SEM images of the individual Ge nanowires and junctions grown on a Si (100) substrate patterned with 150 nm wide slits. The NW growth is guided by the in-plane geometry, with dimensions defined by the substrate patterning. Figure 1a shows the azimuthal dependence of the in-plane NW growth. The inset illustrates the shape of the nanowires in selected directions, for which the faceting will be justified further below. Two preferred orientations lead to smooth faceting along the slits, while the orientations in between result in surface roughening by nanofaceting, as described by Albani et al.[21] Figure 1b and c zoom in to show the structure of growths inside slits oriented along the <100> and <110> directions (see detailed SEM images in the SI). The orientation, size, and length of the slits define the design of the Ge NWs and associated geometries. In principle, there is no limitation in the NW design from the macroscopic point of view. However, defects arising from the lattice mismatch with the substrate as well as from the nanofaceting may be orientation-dependent.

We thus turn to the assessment of the microstructure of the NWs. We performed high-resolution transmission electron microscopy (HRTEM) of the NW cross-sections as a function of their orientation. Figure 2 includes the main characterizations of 80 nm wide NWs grown along the two highly symmetric crystallographic orientations. The 100 nm thick TEM lamellas were prepared by focused ion beam (FIB). Figure 2a and e show the bright field (BF) TEM images of the NW cross-sections acquired perpendicular to the two symmetric growth directions, that is, <110> and <100> orientations, respectively.

Both NW cross-sections exhibit a noninversion symmetric triangular facet morphology, as desired for spin qubit applications.[31] The chemical analysis by energy-dispersive X-ray spectroscopy mapping (EDX) of the cross-sections is shown in Figure 2b and f, confirming the Ge composition and a sharp interface with the Si substrate and SiO_2 mask. We indexed the facets by capturing their relative orientation with the Si (100) substrate. NWs oriented along the <110> direction exhibited well-defined vertically oriented {110} sidewalls, inclined {111} facets at the top corners, and a flat {100}

https://doi.org/10.1021/acs.nanolett.2c00358
Nano Lett. 2022, 22, 4269−4275

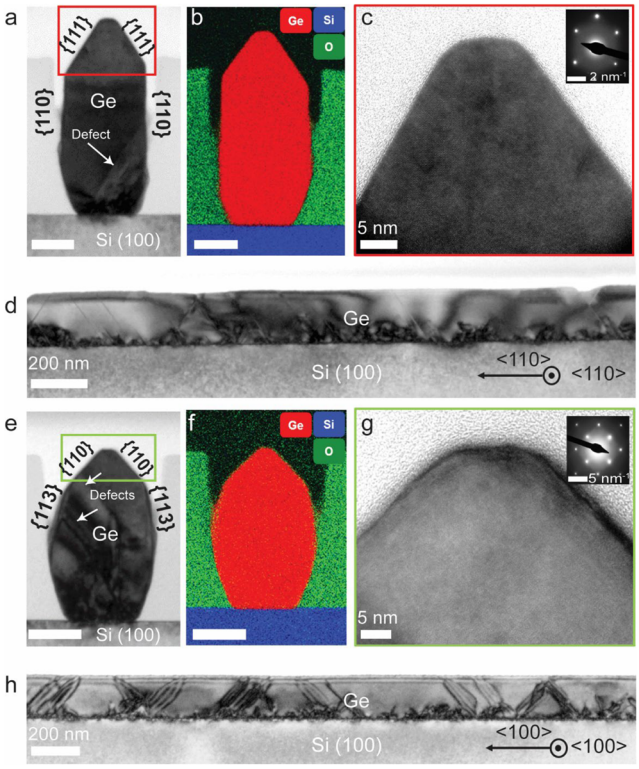

Figure 2. TEM/STEM-EDX images of the in-plane Ge NWs grown along different crystallographic orientations. (a–d) TEM image/STEM-EDX elemental mappings of the NW grown along <110> orientation. (a) BF TEM image of the NW cross-section exhibiting inclined {111} top facets and {110} side facets. (b) EDX elemental mapping showing the elemental distribution. (c) HR-TEM image acquired from the tip of the NW shown in panel a. (d) BF TEM image of the NW cross-section acquired parallel to the NW orientation. (e–h) TEM image/STEM-EDX elemental mappings of the NW grown along <100> orientation. (e) Conventional TEM image of the NW cross-section exhibiting slanted {110} top facets. (f) EDX elemental mapping showing the elemental distribution. (g) HR-TEM image acquired from the tip of the NW shown in panel e. (h) BF TEM image of the NW cross-section acquired parallel to the ridge orientation. The indicated scale bar represents 50 nm.

top facet (Figure 2a). In the case of NWs grown along the <100> directions, the sidewalls belong to the high index {113} family and the inclined top facets to the {110} family (Figure 2e). From a thermodynamic point of view, the facets in the crystal are formed to minimize the total surface energy.[32] Well-defined facets of the {110} family develop along the direction corresponding to the local minimum of the surface energy in the Winterbottom construction.[21,33] Facets of the {113} and {111} families are often observed in regimes highly affected by the kinetics of the system.[13,21] In summary, restricting the in-plane growth of nanowires to different orientations produces nanowires with different cross-sectional morphologies that are determined by the surface energy minimization criterion, interfacial energy, and growth kinetics.

We now proceed with the discussion of the crystal quality by analysis of the BF-TEM micrographs of the NW cross-sections shown in Figure 2a and e. We observe that the NW orientation is directly linked to the crystal quality. For the Ge NWs grown along the <110> direction (Figure 2a), defects generated at the heterostructure interface (indicated by the white arrow) are efficiently trapped by the SiO_2 wall, leaving the upper part of the NW free of defects. Figure 2c presents the HRTEM micrograph obtained from the defect-free region close to the tip of the <110> oriented NW. The selected area electron diffraction (SAED) pattern acquired from the NW tip (Figure 2c, inset) reveals the expected zinc-blende crystal structure of the <110> oriented Ge NWs. In contrast to the NWs grown along the <110> orientation, the NWs grown along the <100> orientation (Figure 2e) exhibited a relatively higher defect density. The majority of the defects formed at the interfaces (indicated by the white arrow) extended into the upper part of the NW. However, we still observe a region free of defects close to the NW tip as shown in the HRTEM image presented in Figure 2g. Similar to <110> oriented NWs, <100> oriented NWs also exhibited a zinc-blende crystal structure as shown in the Figure 3 inset. A comparison of six perpendicular sections of <110> and <100> oriented NWs showed similar behavior (see SI).

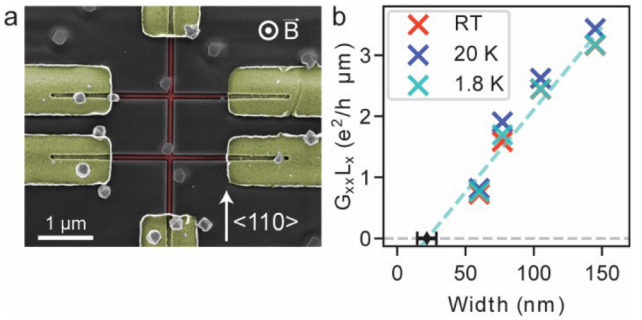

Figure 3. (a) False color SEM image of the nanowire Hall bar device where contacts and nanowire are indicated by gold and red, respectively. Orientation of the main NW axis is indicated by the white arrow. Small bits scattered over the device are Ge parasitic growth on the mask. (b) Normalized conductance $G_{xx}L_x$ as a function of the average NW width measured at T = 1.8 K, 20 K, and room temperature. For the T = 1.8 K data set, a linear fit to the data is shown with a dashed cyan line and the result from the transport cross-section model, twice the depletion width, described in the main text is indicated with a black error bar.

To investigate the presence of defects along the NW length, we made FIB cross-sections parallel to the NW orientation. Figure 2d and h show the BF-TEM image of such parallel cross-sections obtained from <110> and <100> oriented NWs, respectively. Several inclined defects with a spacing ranging between 100 and 500 nm are observed. We suspect these defects to be {111} oriented and their nucleation can be caused due to inhomogeneities on the substrate surface.[30,34−36]

Electrical Transport Measurements. We fabricated four Hall bar devices with <110> and <100> orientation of the main nanowire axis with average widths ranging from ∼60 nm to ∼150 nm. The average width is introduced since NWs do not have a rectangular cross-section (see SI) and we define it as $W_{avg} = \int_0^H w(h)\,dh / \int_0^H dh = A_{c.s.}/H$ where $A_{c.s.}$ and H are the NW cross-section area and height, respectively, and $w(h)$ is the height-dependent nanowire width. In the remaining manuscript, we focus on the transport experiments on <110> NWs (for <100>, see SI).

In Figure 3a, we show an SEM image of the nanowire Hall bar device with Ti (10 nm)/Al (30 nm)/Ti (20 nm)/Au (100 nm) stacks serving as ohmic contacts. A top gate is fabricated on the ∼75 nm wide <110> device by depositing a 35 nm AlO_x ALD layer followed by metal evaporation of 10 nm Ti and 90

https://doi.org/10.1021/acs.nanolett.2c00358
Nano Lett. 2022, 22, 4269−4275

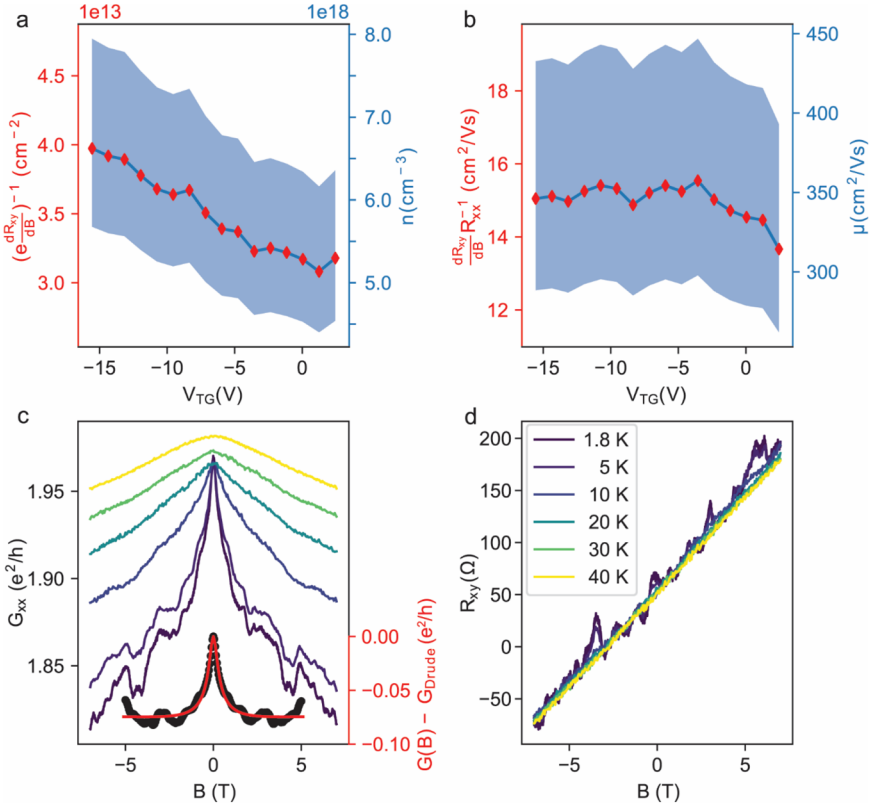

Figure 4. First factor of the (a) density, $(e\ dR_{xy}/dB)^{-1}$, and (b) mobility equation, $(R_{xx}^{-1}dR_{xy}/dB)$, that contains no geometrical assumptions of the NW geometry is plotted in red as a function of the gate voltage with *y*-axis on the left side of the respective figures. Blue shaded regions indicate the corresponding (a) density and (b) mobility range, with *y*-axis on the right side, assuming $H_{eff} = 60 \pm 10$ nm and $W_{eff} = 50 \pm 10$ nm, respectively. (c) G_{xx} as a function of perpendicular magnetic field measured at $T = 1.8$, 5, 10, 20, 30, and 40 K with a waterfall color code scheme. At the bottom of the figure, G_{xx} averaged over the top-gate voltage interval [−1.1 V, 0.4 V] with subtracted background is plotted (black dots) and the corresponding fit (red line) with the corresponding *y*-axis on the right side of the figure. (d) R_{xy} corresponding to the same measurements in panel c.

nm Au. The devices are then measured in a 4-terminal voltage-bias setup using standard low-frequency lock-in techniques with $V_{sd} = 400\ \mu$V in a ^{4}He cryostat with a base temperature of 1.8 K, equipped with temperature control enabling temperatures up to 40 K. Additionally, we investigate the devices using DC measurements in a cryogenic needle prober at room temperature and 20 K.

In Figure 3b, we plot the product $G_{xx}L_x$, of the longitudinal conductance measured on <110> oriented nanowires at 1.8 K, 20 K, and room temperature, and the distance L_x between voltage contacts as a function of the average nanowire width. We observe that temperature has only a small influence on the nanowire conductance. Linearly fitting the data in Figure 3b, we extrapolate to the average width of the NW corresponding to zero conductance and find that nanowires below a width of about 30 nm should not conduct. If we take this value as an estimate of twice the width of a depletion region at the nanowire surface, we get a depletion width of 10−15 nm (see SI).

In addition to this empirical model, we estimated the depletion width by modeling the transport cross-section area as $A_{trans} = A_{c.s.} - C_{c.s.}d$ where $C_{c.s.}$ is the circumference of the wire cross-section and d is the depletion width. Again, similar values are obtained for the depletion width for all temperatures (see SI). In Figure 3b, we indicate both the empirical linear fit (dashed line) and the result of the extended model (black error bar), as an example for the 1.8 K data.

Interestingly, the conductance in all NWs exhibits a small, nonmonotonic temperature dependence. High defect density causes the defect scattering rate $1/\tau_D$ to dominate over the phonon scattering rate $1/\tau_{ph}$ in a large temperature range, causing a small dependence on temperature. This observation indicates that transport may also occur in the part of the NW, which shows many defects in the TEM images (see Figure 2a,e).

From measurements of the Hall (R_{xy}) and longitudinal (R_{xx}) resistance as a function of perpendicular magnetic field B and gate voltage V_G, we can extract density and mobility as a function of V_G (see Figure 4a,b). The data were measured at 1.8 K on a 75 nm wide <110> NW Hall bar and averaged over the gate-voltage interval $\Delta V_G = 1.2\ V$ to suppress the contribution of universal conductance fluctuations (UCF). To extract the density and mobility, an assumption about the effective transport height H_{eff} and width W_{eff} of the nanowire must be made due to the unknown transport cross-section.

Then the Hall-density can be written as $n = (e\ dR_{xy}/dB)^{-1}H_{eff}^{-1}$ where e is the elementary charge. In Figure 4a, we plot on the left axis the first factor of this equation, which contains no geometrical assumptions about H_{eff} and has units of a 2D density, and on the right axis the result of the hole density equation as a density range is indicated with shaded blue region assuming $H_{eff} = 60 \pm 10$ nm (see NW cross-section in SI). The plot indicates a large hole density of $\sim 5 \times 10^{18}$ cm^{-3}, which might be the result of unintentional doping via

https://doi.org/10.1021/acs.nanolett.2c00358
Nano Lett. 2022, 22, 4269−4275

vacancy defects[37] or surface states.[38] Furthermore, the density shows a linear trend in gate voltage from which a 2D capacitance of $\sim 8 \times 10^{-4}$ F/m^2 can be extracted. The extracted capacitance is 50% smaller than a parallel plate capacitance model $\epsilon\epsilon_0/d_{ALD} \approx 1.5 \times 10^{-3}$ F/m^2 would indicate. This is consistent with the notion that transport occurs through the whole cross-sectional area of the nanowire.

In analogy to the extraction of the density, the Drude mobility can be written as a product of an assumption-free factor and a geometry factor, that is, $\mu = (R_{xx}^{-1}\, dR_{xy}/dB)\, L_x/W_{eff}$ where the first factor is plotted on the left axis of Figure 4b and has units of mobility. Assuming $W_{eff} = 50 \pm 10$ nm, and correcting for WAL peak in R_{xx} (see SI), we plot the result of the mobility equation on the right axis of Figure 4b. The range of W_{eff} was chosen such that the extracted mobility fits well with the background of the magnetoconductance (see SI). The extracted mobility is in the range of 300−400 cm^2/(V s) and shows a weak gate-voltage dependence with saturation at $V_G < -5$ V. From n and μ, we extract the Fermi wavelength $\lambda_F \approx 15$ nm and the elastic mean free path $l_e \approx 10$ nm. Such a small l_e is expected due to the high defect density.

Coherent transport phenomena in our devices are probed by magneto-transport measurements (see Figure 4c,d). Universal conductance fluctuations can be seen both in G_{xx} and R_{xy}, indicating coherent transport over a length scale of the order of L_x. From the autocorrelation field of the UCF amplitude ΔG_{xx} at $T = 1.8$ K, we estimate the order of magnitude of the coherence length $l_\phi \approx 100$ nm (see SI). Furthermore, a weak antilocalization (WAL) peak around $B = 0$ T is observed in G_{xx}, suggesting strong spin−orbit interaction. Increasing the temperature leads to a decrease in l_ϕ, most likely caused by an increase in electron−electron scattering. As seen in Figure 4c and d, raising the temperature above 20 K suppresses all interference phenomena and reveals the classical magneto-conductance background. The overall conductance shows a weak increase with temperature which is in accordance with the low extracted $k_F l_e$ and the data in Figure 3b. Similar coherent transport behavior was observed in Hall bar devices with <100> direction as the main growth axis (see SI).

We fit the WAL peak in magneto-conductance $G_{xx}(B)$ in two steps. First, we remove the background by fitting the Drude model expression:

$$G_{Drude} = \frac{G_0}{1 + (\mu B)^2} \tag{1}$$

where G_0, the conductivity at $B = 0$, and μ are the two fitting parameters. The fit is performed at $|B| > 1$ T to exclude the WAL peak from the Drude fit (see SI). Second, we fit the amplitude $\Delta G = G_{xx}(B) - G_{Drude}$ with WAL correction:[39,40]

$$\Delta G = \frac{e^2}{h}\frac{1}{L_x}\left[3\left(\frac{1}{l_\phi^2} + \frac{4}{3l_{SO}^2} + \frac{1}{l_B^2}\right)^{-1/2} - \left(\frac{1}{l_\phi^2} + \frac{1}{l_B^2}\right)^{-1/2} - 3\left(\frac{1}{l_\phi^2} + \frac{3}{l_e^2} + \frac{4}{3l_{SO}^2} + \frac{1}{l_B^2}\right)^{-1/2} + \left(\frac{1}{l_\phi^2} + \frac{3}{l_e^2} + \frac{1}{l_B^2}\right)^{-1/2}\right] \tag{2}$$

where l_{SO} is the spin−orbit length, l_B is the magnetic dephasing length, and h is Planck's constant. The model is valid for a multimode, $\lambda_F < W$, quasi-1D NW, $l_\phi > W$. In the dirty metal regime where $l_e < W$, the magnetic dephasing length is given by $l_B^2 = 3l_m^4/W^2$ where $l_m = \sqrt{\hbar/eB}$ is the magnetic length.

When fitting ΔG, l_ϕ and l_{SO} are the free fitting parameters, and l_e is fixed to 10 nm, while W_{eff} is fixed within the assumed interval. In the inset of Figure 4c, we show the fit to the conductance $G(B)$ trace averaged over the V_G interval [−1.1 V, 0.4 V] for $W_{eff} = 50$ nm. After repeating the fitting procedure for the range of W_{eff}, we obtain $l_\phi \sim 100$ nm, validating the use of the expression for the quasi-1D regime, and $l_{SO} \sim 10$ nm. The extracted l_{SO} is similar to values extracted for holes in Ge/Si core−shell nanowire[41] and smaller than l_{SO} for electrons in InAs nanowires.[42] The similarity between the extracted spin−orbit length and the mean free path, $l_{SO} \approx le$, makes it likely that the Elliott-Yafet mechanism is the dominant spin relaxation mechanism.[43,44]

In summary, we have demonstrated a scalable way to obtain in-plane Ge NWs and their networks on Si substrates with a great degree of controllability over the size, shape, and orientation of the NWs. By employing the selective area growth approach, in plane Ge NWs with well-defined facet morphology were obtained along the highly symmetric crystallographic orientations, that is, <110> and <100>. We investigated transport in NW Hall bar devices and found a high hole density $\sim 5 \times 10^{18}$ cm^{-3}, possibly caused by a large density of vacancy defects or surface states, a weakly top-gate voltage dependent mobility ~400 cm^2/(V s), and the corresponding mean free path $l_e \approx 10$ nm. Together with weak temperature dependence of conductivity, these results indicate that transport may occur both in the defective and defect free part of the nanowire. Magneto-transport measurements showed coherent transport phenomena, UCF, and WAL indicating strong spin−orbit interaction. By fitting WAL, we obtained $l_\phi \approx 100$ nm and $l_{SO} \approx 10$ nm, which point to the Elliott-Yafet mechanism as the dominant spin-relaxation process due to its similarity with the mean free path.

■ ASSOCIATED CONTENT

Supporting Information

The Supporting Information is available free of charge at https://pubs.acs.org/doi/10.1021/acs.nanolett.2c00358.

Substrate preparation methodology, selective area growth parameters, orientation dependency of Ge NW morphology, comments on growth homogeneity, structural characterization on in-plane Ge NWs, details of device fabrication, TEM cross-section of NWs, estimation of depletion width, moility estimation, coherence length from autocorrelation field, weak antilocalization fitting, transport measurements along <110> and <100> oriented nanowires (PDF)

■ AUTHOR INFORMATION

Corresponding Author

Anna Fontcuberta i Morral − *Laboratory of Semiconductor Materials, Institute of Materials, Ecole Polytechnique Fédérale de Lausanne EPFL, Lausanne 1015, Switzerland; Institute of Physics, Faculty of Basic Sciences, Ecole Polytechnique Fédérale de Lausanne EPFL, Lausanne 1015, Switzerland;*

https://doi.org/10.1021/acs.nanolett.2c00358
Nano Lett. 2022, 22, 4269−4275

Center for Quantum Science and Engineering, École Polytechnique Fédérale de Lausanne (EPFL), CH-1015 Lausanne, Switzerland; orcid.org/0000-0002-5070-2196; Email: anna.fontcuberta-morral@epfl.ch

Authors

Santhanu Panikar Ramanandan − *Laboratory of Semiconductor Materials, Institute of Materials, Ecole Polytechnique Fédérale de Lausanne EPFL, Lausanne 1015, Switzerland;* orcid.org/0000-0003-2832-8641

Petar Tomić − *Solid State Laboratory, ETH Zurich, 8093 Zurich, Switzerland;* orcid.org/0000-0001-7634-2136

Nicholas Paul Morgan − *Laboratory of Semiconductor Materials, Institute of Materials, Ecole Polytechnique Fédérale de Lausanne EPFL, Lausanne 1015, Switzerland*

Andrea Giunto − *Laboratory of Semiconductor Materials, Institute of Materials, Ecole Polytechnique Fédérale de Lausanne EPFL, Lausanne 1015, Switzerland*

Alok Rudra − *Laboratory of Semiconductor Materials, Institute of Materials, Ecole Polytechnique Fédérale de Lausanne EPFL, Lausanne 1015, Switzerland*

Klaus Ensslin − *Solid State Laboratory, ETH Zurich, 8093 Zurich, Switzerland; Quantum Center, ETH Zurich, CH-8093 Zurich, Switzerland*

Thomas Ihn − *Solid State Laboratory, ETH Zurich, 8093 Zurich, Switzerland; Quantum Center, ETH Zurich, CH-8093 Zurich, Switzerland*

Complete contact information is available at: https://pubs.acs.org/10.1021/acs.nanolett.2c00358

Author Contributions

#S.P.R. and P.T. contributed equally to this work. S.P.R. performed the substrate fabrication, growth of NWs, structural and morphological characterization, and wrote the corresponding parts of the manuscript. P.T. fabricated the top gated devices and performed the electrical characterization, magneto transport measurements, and wrote the corresponding section of the manuscript. N.P.M. participated with the substrate fabrication and assisted with growth experiments. A.R. significantly participated in optimizing the growth of Ge NWs. A.G. participated in growth discussions and assisted with the growth. A.F.i.M., T.I., and K.E. supervised the work and provided valuable input throughout the project and in manuscript writing. All authors commented on the work and approved the final version of the manuscript.

Notes

The authors declare no competing financial interest.

■ ACKNOWLEDGMENTS

This work was supported as a part of NCCR SPIN, a National Centre of Competence (or Excellence) in Research, funded by the Swiss National Science Foundation (Grant No. 51NF40-180604). The authors from EPFL further acknowledge funding from Innosuisse through project LiD and NCCR QSIT.

■ REFERENCES

(1) Scappucci, G.; Kloeffel, C.; Zwanenburg, F. A.; Loss, D.; Myronov, M.; Zhang, J.-J.; De Franceschi, S.; Katsaros, G.; Veldhorst, M. The Germanium Quantum Information Route. *Nat. Rev. Mater.* **2021**, *6* (10), 926−943.

(2) Kloeffel, C.; Trif, M.; Loss, D. Strong Spin-Orbit Interaction and Helical Hole States in Ge/Si Nanowires. *Phys. Rev. B* **2011**, *84* (19), 195314.

(3) Higginbotham, A. P.; Kuemmeth, F.; Larsen, T. W.; Fitzpatrick, M.; Yao, J.; Yan, H.; Lieber, C. M.; Marcus, C. M. Antilocalization of Coulomb Blockade in a Ge/Si Nanowire. *Phys. Rev. Lett.* **2014**, *112* (21), 216806.

(4) Jirovec, D.; Hofmann, A.; Ballabio, A.; Mutter, P. M.; Tavani, G.; Botifoll, M.; Crippa, A.; Kukucka, J.; Sagi, O.; Martins, F.; Saez-Mollejo, J.; Prieto, I.; Borovkov, M.; Arbiol, J.; Chrastina, D.; Isella, G.; Katsaros, G. A Singlet-Triplet Hole Spin Qubit in Planar Ge. *Nat. Mater.* **2021**, *20* (8), 1106−1112.

(5) Aggarwal, K.; Hofmann, A.; Jirovec, D.; Prieto, I.; Sammak, A.; Botifoll, M.; Marti-Sanchez, S.; Veldhorst, M.; Arbiol, J.; Scappucci, G.; Danon, J.; Katsaros, G. Enhancement of Proximity Induced Superconductivity in a Planar Ge Hole Gas. *Phys. Rev. Res.* **2021**, *3* (2), L022005.

(6) Bosco, S.; Loss, D. Fully Tunable Hyperfine Interactions of Hole Spin Qubits in Si and Ge Quantum Dots. *Phys. Rev. Lett.* **2021**, *127* (19), 190501.

(7) Froning, F. N. M.; Camenzind, L. C.; van der Molen, O. A. H.; Li, A.; Bakkers, E. P. A. M.; Zumbühl, D. M.; Braakman, F. R. Ultrafast Hole Spin Qubit with Gate-Tunable Spin−Orbit Switch Functionality. *Nat. Nanotechnol.* **2021**, *16* (3), 308−312.

(8) Watzinger, H.; Kukučka, J.; Vukušić, L.; Gao, F.; Wang, T.; Schäffler, F.; Zhang, J. J.; Katsaros, G. A Germanium Hole Spin Qubit. *Nat. Commun.* **2018**, *9* (1), 2−7.

(9) Car, D.; Wang, J.; Verheijen, M. A.; Bakkers, E. P. A. M.; Plissard, S. R. Rationally Designed Single-Crystalline Nanowire Networks. *Adv. Mater.* **2014**, *26* (28), 4875−4879.

(10) Gazibegovic, S.; Car, D.; Zhang, H.; Balk, S. C.; Logan, J. A.; de Moor, M. W. A.; Cassidy, M. C.; Schmits, R.; Xu, D.; Wang, G.; Krogstrup, P.; Op het Veld, R. L. M.; Zuo, K.; Vos, Y.; Shen, J.; Bouman, D.; Shojaei, B.; Pennachio, D.; Lee, J. S.; van Veldhoven, P. J.; Koelling, S.; Verheijen, M. A.; Kouwenhoven, L. P.; Palmstrøm, C. J.; Bakkers, E. P. A. M. Epitaxy of Advanced Nanowire Quantum Devices. *Nature* **2017**, *548* (7668), 434−438.

(11) Krizek, F.; Kanne, T.; Razmadze, D.; Johnson, E.; Nygård, J.; Marcus, C. M.; Krogstrup, P. Growth of InAs Wurtzite Nanocrosses from Hexagonal and Cubic Basis. *Nano Lett.* **2017**, *17* (10), 6090−6096.

(12) Collins, C. B.; Carlson, R. O.; Gallagher, C. J. Properties of Gold-Doped Silicon. *Phys. Rev.* **1957**, *105* (4), 1168−1173.

(13) Friedl, M.; Cerveny, K.; Weigele, P.; Tutuncuoglu, G.; Marti-Sanchez, S.; Huang, C.; Patlatiuk, T.; Potts, H.; Sun, Z.; Hill, M. O.; Guniat, L.; Kim, W.; Zamani, M.; Dubrovskii, V. G.; Arbiol, J.; Lauhon, L. J.; Zumbuhl, D. M.; Fontcuberta i Morral, A. Template-Assisted Scalable Nanowire Networks. *Nano Lett.* **2018**, *18* (4), 2666−2671.

(14) Aseev, P.; Fursina, A.; Boekhout, F.; Krizek, F.; Sestoft, J. E.; Borsoi, F.; Heedt, S.; Wang, G.; Binci, L.; Martí-Sánchez, S.; Swoboda, T.; Koops, R.; Uccelli, E.; Arbiol, J.; Krogstrup, P.; Kouwenhoven, L. P.; Caroff, P. Selectivity Map for Molecular Beam Epitaxy of Advanced III−V Quantum Nanowire Networks. *Nano Lett.* **2019**, *19* (1), 218−227.

(15) Krizek, F.; Sestoft, J. E.; Aseev, P.; Marti-Sanchez, S.; Vaitiekenas, S.; Casparis, L.; Khan, S. A.; Liu, Y.; Stankevič, T.; Whiticar, A. M.; Fursina, A.; Boekhout, F.; Koops, R.; Uccelli, E.; Kouwenhoven, L. P.; Marcus, C. M.; Arbiol, J.; Krogstrup, P. Field Effect Enhancement in Buffered Quantum Nanowire Networks. *Phys. Rev. Mater.* **2018**, *2* (9), 1−8.

(16) Aseev, P.; Wang, G.; Binci, L.; Singh, A.; Martí-Sánchez, S.; Botifoll, M.; Stek, L. J.; Bordin, A.; Watson, J. D.; Boekhout, F.; Abel, D.; Gamble, J.; Van Hoogdalem, K.; Arbiol, J.; Kouwenhoven, L. P.; de Lange, G.; Caroff, P. Ballistic InSb Nanowires and Networks via Metal-Sown Selective Area Growth. *Nano Lett.* **2019**, *19* (12), 9102−9111.

(17) Gao, F.; Wang, J.; Watzinger, H.; Hu, H.; Rančić, M. J.; Zhang, J.; Wang, T.; Yao, Y.; Wang, G.; Kukučka, J.; Vukušić, L.; Kloeffel, C.; Loss, D.; Liu, F.; Katsaros, G.; Zhang, J. Site-Controlled Uniform Ge/Si Hut Wires with Electrically Tunable Spin−Orbit Coupling. *Adv. Mater.* **2020**, *32* (16), 1906523.

(18) Adelsberger, C.; Benito, M.; Bosco, S.; Klinovaja, J.; Loss, D. Hole-Spin Qubits in Ge Nanowire Quantum Dots: Interplay of Orbital Magnetic Field, Strain, and Growth Direction. *Phys. Rev. B* **2022**, *105* (7), No. 075308.
(19) Yuan, X.; Pan, D.; Zhou, Y.; Zhang, X.; Peng, K.; Zhao, B.; Deng, M.; He, J.; Tan, H. H.; Jagadish, C. Selective Area Epitaxy of III−V Nanostructure Arrays and Networks: Growth, Applications, and Future Directions. *Appl. Phys. Rev.* **2021**, *8* (2), No. 021302.
(20) Heiß, M.; Riedlberger, E.; Spirkoska, D.; Bichler, M.; Abstreiter, G.; Morral, A. F. i. Growth Mechanisms and Optical Properties of GaAs-Based Semiconductor Microstructures by Selective Area Epitaxy. *J. Cryst. Growth* **2008**, *310* (6), 1049−1056.
(21) Albani, M.; Ghisalberti, L.; Bergamaschini, R.; Friedl, M.; Salvalaglio, M.; Voigt, A.; Montalenti, F.; Tütüncüoglu, G.; Fontcuberta i Morral, A.; Miglio, L. Growth Kinetics and Morphological Analysis of Homoepitaxial GaAs Fins by Theory and Experiment. *Phys. Rev. Mater.* **2018**, *2* (9), No. 093404.
(22) Yang, Z.; Surrente, A.; Tutuncuoglu, G.; Galkowski, K.; Cazaban-Carrazé, M.; Amaduzzi, F.; Leroux, P.; Maude, D. K.; Fontcuberta I Morral, A.; Plochocka, P. Revealing Large-Scale Homogeneity and Trace Impurity Sensitivity of GaAs Nanoscale Membranes. *Nano Lett.* **2017**, *17* (5), 2979−2984.
(23) Park, J. S.; Bai, J.; Curtin, M.; Adekore, B.; Carroll, M.; Lochtefeld, A. Defect Reduction of Selective Ge Epitaxy in Trenches on Si(001) Substrates Using Aspect Ratio Trapping. *Appl. Phys. Lett.* **2007**, *90* (5), 1−4.
(24) Li, J. Z.; Bai, J.; Major, C.; Carroll, M.; Lochtefeld, A.; Shellenbarger, Z. Defect Reduction of GaAs/Si Epitaxy by Aspect Ratio Trapping. *J. Appl. Phys.* **2008**, *103* (10), 106102.
(25) Wang, G.; Leys, M. R.; Loo, R.; Richard, O.; Bender, H.; Waldron, N.; Brammertz, G.; Dekoster, J.; Wang, W.; Seefeldt, M.; Caymax, M.; Heyns, M. M. Selective Area Growth of High Quality InP on Si (001) Substrates. *Appl. Phys. Lett.* **2010**, *97* (12), 1−4.
(26) Friedl, M.; Cerveny, K.; Weigele, P.; Tutuncuoglu, G.; Marti-Sanchez, S.; Huang, C.; Patlatiuk, T.; Potts, H.; Sun, Z.; Hill, M. O.; Guniat, L.; Kim, W.; Zamani, M.; Dubrovskii, V. G.; Arbiol, J.; Lauhon, L. J.; Zumbuhl, D. M.; Fontcuberta i Morral, A. Template-Assisted Scalable Nanowire Networks. *Nano Lett.* **2018**, *18* (4), 2666−2671.
(27) Op het Veld, R. L. M.; Xu, D.; Schaller, V.; Verheijen, M. A.; Peters, S. M. E.; Jung, J.; Tong, C.; Wang, Q.; de Moor, M. W. A.; Hesselmann, B.; Vermeulen, K.; Bommer, J. D. S.; Sue Lee, J.; Sarikov, A.; Pendharkar, M.; Marzegalli, A.; Koelling, S.; Kouwenhoven, L. P.; Miglio, L.; Palmstrøm, C. J.; Zhang, H.; Bakkers, E. P. A. M. In-Plane Selective Area InSb−Al Nanowire Quantum Networks. *Commun. Phys.* **2020**, *3* (1), 59.
(28) Nam, J. H.; Alkis, S.; Nam, D.; Afshinmanesh, F.; Shim, J.; Park, J.-H.; Brongersma, M.; Okyay, A. K.; Kamins, T. I.; Saraswat, K. Lateral Overgrowth of Germanium for Monolithic Integration of Germanium-on-Insulator on Silicon. *J. Cryst. Growth* **2015**, *416*, 21−27.
(29) Wen, R.-T.; Wang, B.; Michel, J. Unpredicted Internal Geometric Reconfiguration of an Enclosed Space Formed by Heteroepitaxy. *Nano Lett.* **2020**, *20* (1), 540−545.
(30) Li, Q.; Han, S. M.; Brueck, S. R. J.; Hersee, S.; Jiang, Y.-B.; Xu, H. Selective Growth of Ge on Si(100) through Vias of SiO2 Nanotemplate Using Solid Source Molecular Beam Epitaxy. *Appl. Phys. Lett.* **2003**, *83* (24), 5032−5034.
(31) Bosco, S.; Hetényi, B.; Loss, D. Hole Spin Qubits in Si FinFETs With Fully Tunable Spin-Orbit Coupling and Sweet Spots for Charge Noise. *PRX Quantum* **2021**, *2* (1), No. 010348.
(32) Wang, N.; Wong, W. W.; Yuan, X.; Li, L.; Jagadish, C.; Tan, H. H. Understanding Shape Evolution and Phase Transition in InP Nanostructures Grown by Selective Area Epitaxy. *Small* **2021**, *17* (21), 1−12.
(33) Kaplan, W. D.; Chatain, D.; Wynblatt, P.; Carter, W. C. A Review of Wetting versus Adsorption, Complexions, and Related Phenomena: The Rosetta Stone of Wetting. *J. Mater. Sci.* **2013**, *48* (17), 5681−5717.
(34) Scappucci, G.; Kloeffel, C.; Zwanenburg, F. A.; Loss, D.; Myronov, M.; Zhang, J.-J.; De Franceschi, S.; Katsaros, G.; Veldhorst, M. The Germanium Quantum Information Route. *Nat. Rev. Mater.* **2021**, *6* (10), 926−943.
(35) Van Thourhout, D.; Shi, Y.; Baryshnikova, M.; Mols, Y.; Kuznetsova, N.; De Koninck, Y.; Pantouvaki, M.; Van Campenhout, J.; Langer, R.; Kunert, B. Nano-Ridge Laser Monolithically Grown on (001) Si. *Semiconductors and Semimetals* **2019**, *101*, 283−304, DOI: 10.1016/bs.semsem.2019.07.002.
(36) Kunert, B.; Mols, Y.; Baryshniskova, M.; Waldron, N.; Schulze, A.; Langer, R. How to Control Defect Formation in Monolithic III/V Hetero-Epitaxy on (100) Si? A Critical Review on Current Approaches. *Semicond. Sci. Technol.* **2018**, *33* (9), No. 093002.
(37) Fage-Pedersen, J.; Nylandsted Larsen, A.; Mesli, A. Irradiation-Induced Defects in Ge Studied by Transient Spectroscopies. *Phys. Rev. B - Condens. Matter Mater. Phys.* **2000**, *62* (15), 10116−10125.
(38) Zhang, S.; Hemesath, E. R.; Perea, D. E.; Wijaya, E.; Lensch-Falk, J. L.; Lauhon, L. J. Relative Influence of Surface States and Bulk Impurities on the Electrical Properties of Ge Nanowires. *Nano Lett.* **2009**, *9* (9), 3268−3274.
(39) Kurdak, Ç.; Chang, A. M.; Chin, A.; Chang, T. Y. Quantum Interference Effects and Spin-Orbit Interaction in Quasi-One-Dimensional Wires and Rings. *Phys. Rev. B* **1992**, *46* (11), 6846−6856.
(40) van Weperen, I.; Tarasinski, B.; Eeltink, D.; Pribiag, V. S.; Plissard, S. R.; Bakkers, E. P. A. M.; Kouwenhoven, L. P.; Wimmer, M. Spin-Orbit Interaction in InSb Nanowires. *Phys. Rev. B* **2015**, *91* (20), 201413.
(41) Hao, X. J.; Tu, T.; Cao, G.; Zhou, C.; Li, H. O.; Guo, G. C.; Fung, W. Y.; Ji, Z.; Guo, G. P.; Lu, W. Strong and Tunable Spin-Orbit Coupling of One-Dimensional Holes in Ge/Si Core/Shell Nanowires. *Nano Lett.* **2010**, *10* (8), 2956−2960.
(42) Liang, D.; Gao, X. P. A. Strong Tuning of Rashba Spin-Orbit Interaction in Single InAs Nanowires. *Nano Lett.* **2012**, *12* (6), 3263−3267.
(43) Žutić, I.; Fabian, J.; Das Sarma, S. Spintronics: Fundamentals and Applications. *Rev. Mod. Phys.* **2004**, *76* (2), 323−410.
(44) Patibandla, S.; Pramanik, S.; Bandyopadhyay, S.; Tepper, G. C. Spin Relaxation in a Germanium Nanowire. *J. Appl. Phys.* **2006**, *100* (4), No. 044303.

https://doi.org/10.1021/acs.nanolett.2c00358
Nano Lett. 2022, 22, 4269−4275